Electron transfer dynamics of quaternary sulfur semiconductor/mos$_2$ layer-on-layer for efficient visible-light h$_2$ evolution

Xiaowei Shi, Mamoru Fujitsuka, Tetsuro Majima*

The Institute of Scientific and Industrial Research (SANKEN), Osaka University, Mihogaoka 8-1, Ibaraki, Osaka, 567-0047, Japan

ABSTRACT

Photocatalytic water reduction into H$_2$ provides huge charm for simultaneously resolving fossil energy shortage and environmental issues. Seeking photocatalysts with characteristics of low-cost, environmental friendliness and visible light response, and accelerating the charge separation remain significant challenges to develop high efficient solar-to-H$_2$ conversion systems. Here, quaternary sulfur semiconductor Zn$_{0.4}$Ca$_{0.6}$In$_2$S$_4$ (ZCIS) micro-spheres composed of cross-linked nanosheets and ZCIS microspheres modified with MoS$_2$ (ZM-*X*) were designed and prepared *via* hydrothermal methods. Detailed characterizations indicated that the layer structured MoS$_2$ nanosheets were mainly deposited on the surface of ZCIS nanosheet to form a 2D-2D structure that greatly increased the contact surface area for charge transfer, which was critical to the high photocatalytic performance for H$_2$ evolution. Femtosecond time-resolved diffuse reflectance spectroscopy was used to evaluate the transfer dynamics of photogenerated electrons in ZCIS and ZM-*X* and revealed that an additional decay route within 5 ps for the photogenerated electrons in ZCIS after combining with MoS$_2$ appeared which could be ascribed to the electron injection from ZCIS to MoS$_2$. In addition, it was also demonstrated that ZM-3.0 (ZCIS with 3 wt% MoS$_2$ loading amount) exhibited the fastest electron injection within only 1.12 ps and the highest efficient injection efficiency of 69.9%. As a result, ZM-3.0 exhibited the evolution rate of 3.5 μmol h^{-1} under visible light irradiation ($\lambda \geq 420$ nm), which was 27 times higher than that of ZCIS (0.13 μmol h^{-1}). The results indicate that the quaternary sulfur semiconductor has great potential as a new kind of photocatalysts for solar energy conversion.

1. Introduction

Due to the massive combustion of fossil fuel, the shortage of fossil resources and increased environment crisis begin to restrain further development of the society. Conversion of water to H$_2$ utilizing solar energy by photocatalysts is of great potential, which not only supplies green energy source for industrial but also shrinks the generation of contaminative gases thus attracting enormous research interests recently [1,2]. Until now, numerous active photocatalysts including metal/metallic oxides, nitrides, and transition metal sulfides, have been developed for the aforementioned photocatalytic reaction [3–5]. Since the visible light covers 42–43% of the solar light, most attentions are now focused on the synthesis of efficient visible-light driven photocatalysts [4,6,7]. In recent years, quaternary oxide (or sulfide) semiconductors have become promising candidates for photocatalysis reactions owing to their suitable band gap and considerable chemical stabilities [8–10]. It has been reported that the quaternary oxide semiconductor (β-AgAl$_{1-x}$Ga$_x$O$_2$) exhibits much higher photocatalytic performance in iso-propanol photodegradation under visible light

irradiation [10]. However, this kind of quaternary sulfide semi-conductors have been seldomly used as solar-driven photocatalysts for H$_2$ evolution.

Similar to the ternary sulfide semiconducors, quaternary sulfide photocatalysts may also suffer the shortcomings for H$_2$ evolution, such as quick recombination of photogenerated electron-hole pairs and lack of active sites [11,12]. Recently, two-dimensional MoS$_2$ nanosheet, composed of three stacked atom layers (S-Mo-S) held together by van der Waals forces, has been extensively studied and attracts much attention toward H$_2$ evolution [13–16]. Through the density functional theory calculations on free energy, it indicates that MoS$_2$ has the free energy close to zero when MoS$_2$ is worked as the catalyst for H$_2$ evolution, which is the same as the case of Pt [17]. In addition, because the sulfur atoms on exposed edges could serve as active sites for photocatalysis reaction, MoS$_2$ is shown to be a promising and low-cost candidate cocatalyst instead of Pt [17]. Zhou et al. indicated that TiO$_2$@MoS$_2$ heterostructure with 50 wt% MoS$_2$ exhibited the highest photocatalytic H$_2$ evolution [18]. Li et al. also reported that MoS$_2$/RGO hybrid catalyst showed excellent electrocatalytic H$_2$ evolution rate [14].

Theoretically, the active sulfur atoms of MoS_2 only locate on the exposed edges, while the sulfurs on the basal plane are catalytically inert. As a result, nanosized MoS_2 with more exposed edges and active sulfur atoms should be more active for H_2 evolution than materials in bulk forms.

Femtosecond time-resolved transient absorption (fs-TAS) has been widely used to deeply investigate the migration and recombination dynamics of photogenerated charge carrier in semiconductors within picosecond time scale [19–21], and is employed here to help us explore the fundamental reasons for the enhancement of photocatalytic activity. It has been reported that the conduction band (CB) level of the quaternary sulfur semiconductors could be gradually shifted by changing amount of new introducing element [8]. As is well known, the photoreduction ability of a semiconductor is closely related with its CB position, and a higher CB level provides a larger reduction diving force [22]. Further functionalization of the quaternary sulfur semiconductor with MoS_2 greatly enhances the charge separation efficiency and thus improves its photocatalytic activity.

Herein, we report a photocatalytic H_2 evolution by $ZnIn_2S_4$-based quaternary sulfur semiconductor, $Zn_{0.4}Ca_{0.6}In_2S_4$ (ZCIS) microspheres composed of cross-linked nanosheets, combined with MoS_2 by hydrothermal process. Layer structured MoS_2 were mostly deposited on the surface of ZCIS nanosheets to form a 2D-2D structure. As expected, the photocatalytic activity of ZCIS was greatly enhanced under visible light irradiation after loading MoS_2 compared with the bare one. According to the results of photoelectrochemical spectroscopy and fs-TAS, charge separation and electron injection dynamics, injection rate, and injection efficiency of the photocatalysts were explored. Proper mechanisms were proposed to account for the improved photocatalytic H_2 evolution activity of various photocatalytic materials. The present results may inspire the exploration of low-cost efficient photocatalysts for water splitting.

2. Experimental section

2.1. Preparation of ZCIS and ZM-X

ZCIS was prepared by a hydrothermal process according to previous work [8]. $ZnCl_2$ (27 mg), $Ca(NO_3)_2 \cdot 4H_2O$ (71 mg), $InCl_3 \cdot 4H_2O$ (293 mg), and thioacetamide (TAA 150 mg) were dissolved in 25 mL deionized water and 5 mL of glycol. After stirring for about 30 min at room temperature, the resulting heterogeneous solution was transferred into a 50 mL Teflon-lined stainless steel autoclave and maintained at 120 °C for 12 h in an oven. The products were collected by centrifugation and dried at 60 °C oven. For synthesis of ZM-X (X = 0.6, 1.8, 3.0, 4.2, and 6.0, representing the weight percentage of MoS_2), different amount of $(NH_4)_2MoS_4$ and 100 mg ZCIS were added to 12.5 mL DMF and then stirred for 30 min under room temperature. Then the homogeneous solution was transferred to a 50 mL Teflon-lined autoclave and maintained at 200 °C for 10 h. The products were collected by centrifugation and dried. Pure MoS_2 was synthesized without adding ZCIS.

2.2. Photocatalytic H_2 evolution

3 mg sample were dispersed in 5 mL aqueous solution containing 20 vol% lactic acid for H_2 evolution. Prior to the irradiation, the catalyst was dispersed using an ultrasonic bath, and then bubbled with argon through the reactor for 30 min to completely remove the dissolved oxygen and ensure the reactor was in an anaerobic condition. The samples were irradiated at different wavelengths using a Xenon lamp for H_2 evolution (Asahi Spectra, HAL-320; 300 mW cm^{-2}). The reaction temperature was kept at about 293 K. The visible light was filtered with a nominal 420 nm cutoff filter. The volume of H_2 was measured by using a Shimadzu GC-8A gas chromatograph equipped with an MS-5A column and a thermal conductivity detector. The catalytic stability was evaluated by isolating, washing and reusing the

catalyst in a cycling experiment. The apparent quantum efficiency (AQE) was calculated using the following equation [23],

$$AQE\,(\%) = \frac{\text{Number of evolved }H_2\text{ molecules} \times 2}{\text{Number of incident photons}} \times 100\%.$$

2.3. Photoelectrochemical measurements

Electrochemical and photoelectrochemical measurements were performed in a three-electrode quartz cell. A Platinum wire was used as the counter electrode, and an Ag/AgCl electrode was used as the reference electrodes. For loading sample on a glassy carbon electrode, 4 mg sample was added into solution containing H_2O and CH_3CH_2OH with volume ratio of 1:1. Then 50 μL Nafion was added into the solution. After ultrasonic for 10 min, 3 μL solution was took out and drop on the surface of glassy carbon. The electrode was used for photoelectrochemical measurements after drying. 0.1 M Na_2SO_4 aqueous solution was used as the electrolyte. Electrochemical impedance spectroscopy (EIS) was carried out under visible light irradiation. A Xenon lamp was utilized as the light source in the photoelectrochemical measurements with the intensity of 300 mW cm^{-2} and the visible light was filtered with nominal 420 nm cutoff filter. The potential (vs. Ag/AgCl) was converted to the reversible hydrogen electrode (RHE) according to the Nernst equation:

$$E_{RHE} = E + 0.05916 pH + E_0$$

where E_{RHE} is the potential vs. RHE, $E_0 = 0.1976$ V at 25 °C, and E is the measured potential vs. Ag/AgCl.

2.4. Time-resolved diffuse reflectance measurements

The femtosecond diffuse reflectance spectra were measured by the pump and probe method using a regeneratively amplified titanium sapphire laser (Spectra-Physics, Spitfire Pro F, 1 kHz) pumped by a Nd:YLF laser (Spectra-Physics, Empower 15). The output of an optical parametric amplifier (420 nm, 4 μJ pulse^{-1}) was used as the excitation pulse. A white light continuum pulse, which was generated by focusing the residual of the fundamental light on a sapphire crystal, was directed to the sample powder coated on the glass substrate, and the reflected lights were detected by a linear InGaAs array detector equipped with the polychromator (Solar, MS3504). All measurements were carried out at room temperature.

2.5. Characterization of materials

The samples were characterized using X-ray diffraction (XRD, Rigaku Rint-2500, CuKα source), and HRTEM (JEOL JEM 3000 F, operated at 300 kV). The steady-state UV–vis absorption and diffuse reflectance spectra were measured by UV–vis-NIR spectrophotometers (Shimadzu UV-3100 and Jasco V-570) at room temperature. XPS measurements were performed with a PHI X-tool 8ULVAC-PHI.

3. Results and discussion

Crystal structure of the prepared samples was first examined by X-ray diffraction (XRD). The patterns shown in Fig. 1 demonstrate that the main peaks at 21.2, 27.3, 30.5, 47.0, 52.2, 55.4, and 75.9° are consistent with previous reports, indicating the successful synthesis of $Zn_{0.4}Ca_{0.6}In_2S_4$ (ZCIS) [8]. And no peak around 33.0° indicates the trigonal crystal system of ZCIS [8]. No other characteristic peaks are found, evidencing the high purity of ZCIS. Due to the small loading amount, the peaks of MoS_2 could not be observed in ZM-X samples. In addition, HRTEM and elemental mapping were further used to prove the formation of ZCIS (Fig. S1). As revealed by HRTEM images, ZCIS exhibits a flower-like microsphere morphology made up by many cross-linked nanosheets and the lattice fringe with intervals of 0.330 nm is
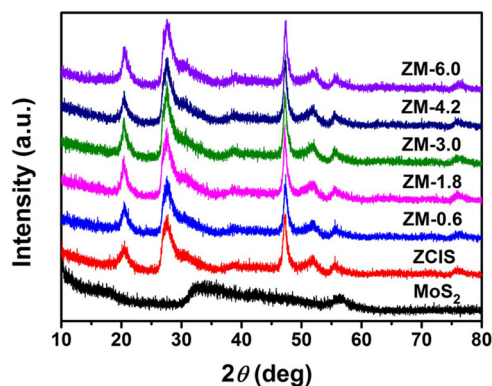
Fig. 1. XRD patterns of MoS_2, ZCIS, and ZM-*X*.

attributed to the (110) plane. The elemental mapping suggests that Zn, Ca, In, and S elements have a highly homogeneous distribution throughout ZCIS microsphere. XRD and HRTEM image results evident that ZCIS is successfully obtained by the hydrothermal method.

The morphology and structure of as-prepared samples were characterized by SEM and HRTEM. SEM image of ZCIS in Fig. S2A shows the homogeneously distributed microsphere morphology with the size in the range of 4–8 μm. ZM-*X* samples still kept a microsphere morphology and size similar to pure ZCIS after loading MoS_2. It is clearly shown that no MoS_2 could be observed due to the limited loading amount of MoS_2 (less than 3.0 wt%). However, MoS_2 aggregated nanoflowers start to appear if further increasing the amount, as shown in the red circles in Figs. S2E and F, which is similar to pure MoS_2 without adding ZCIS precursors (Fig. S3). HRTEM image in Fig. 2 presents detailed crystal information of ZM-3.0. The lattice fringes with a distance of 0.330 nm

corresponds to the (110) plane of ZCIS, implying a preserved crystal structure after second hydrothermal process. Short-range lattice fringes with distance of 0.62 nm are also observed, which is consistent with the d-spacing of (002) planes of MoS_2 [13]. The close 2D-2D interface contact between ZCIS and MoS_2 favors the transportation of photogenerated charges.

To identify the composition and surface chemical states of representative elements of ZCIS and ZM-*X* samples, XPS measurements were carried out. Survey spectra of ZCIS and ZM-3.0 are first shown in Fig. S4. The high resolution XPS spectrum for Zn 2p in ZCIS (Fig. 3A) shows two peaks at 1045.3 and 1022.4 eV attributable to Zn^{2+} $2p_{1/2}$ and $2p_{3/2}$, respectively. In the XPS spectrum for In 3d of ZCIS (Fig. 3B), peaks at 453.1 and 445.5 eV are assigned to In $3d_{3/2}$ and In $3d_{5/2}$, respectively. While compared with ZCIS, the peak positions of Zn 2p and In 3d in ZM-3.0 sample shift to lower binding energies by approximately 0.3 and 0.7 eV, respectively. Mo 3d XPS spectrum of ZM-3.0 shows two peaks centered at 228.7 and 232.0 eV (Fig. 3C), assigned to Mo $3d_{5/2}$ and Mo $3d_{3/2}$, respectively, demonstrating that Mo is in the + 4 valence state. Contrary to the peak shift of Zn 2p and In 3d, the peak positions of Mo 3d in ZM-3.0 move to the higher binding energy (about 0.5 eV). This peak shift toward lower binding energy, suggesting a strong interaction between MoS_2 and ZCIS, is ascribed to the increase of electron concentration with enhanced electron screening effect caused by the formation of ZCIS/MoS_2 junction. The binding energies of S^{2-} $2p_{1/2}$ and $2p_{3/2}$ orbitals for ZCIS are 162.6 and 161.5 eV, and those for MoS_2 are 162.7 and 161.7 eV, respectively, which are in accordance with previous reported results [8,23].

Optical absorption spectra of photocatalysts, playing a significant role for photocatalytic performance of semiconductors, were measured by diffuse reflection spectroscopy (DRS). Fig. 4A depicts DRS spectra for ZCIS and ZM-*X* and all samples exhibit photoresponse in visible region.
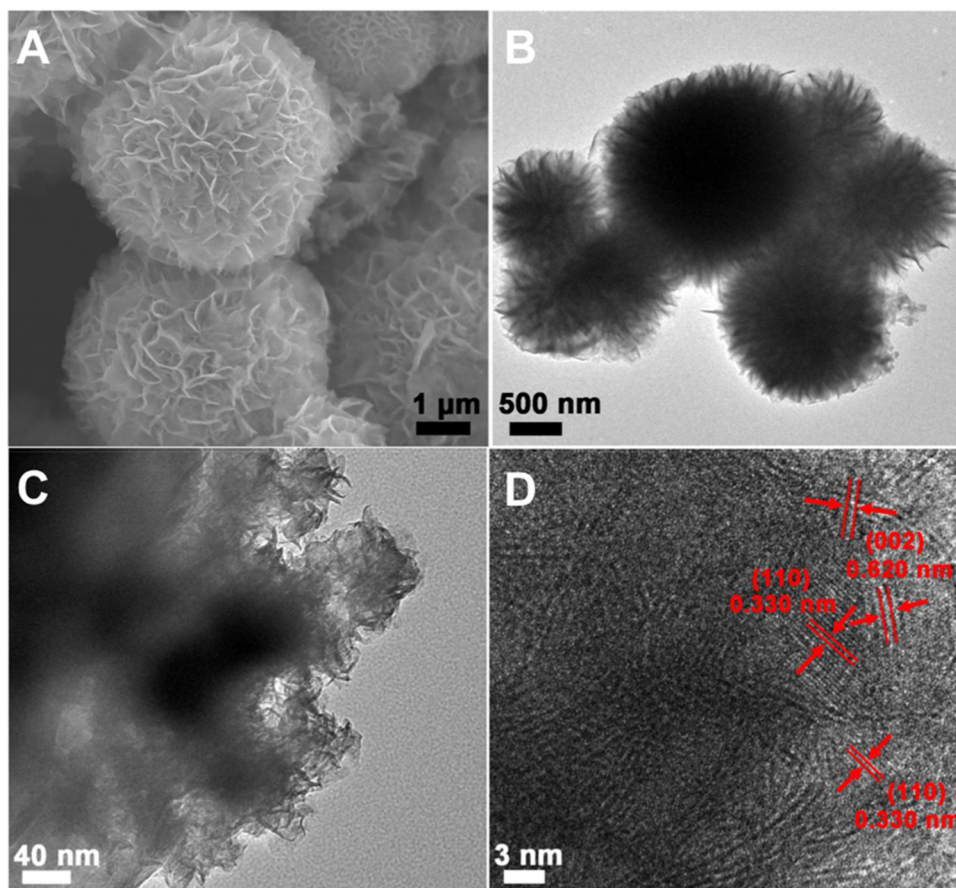

Fig. 2. SEM image (A), TEM images (B–C), and HRTEM image (D) of ZM-3.0.
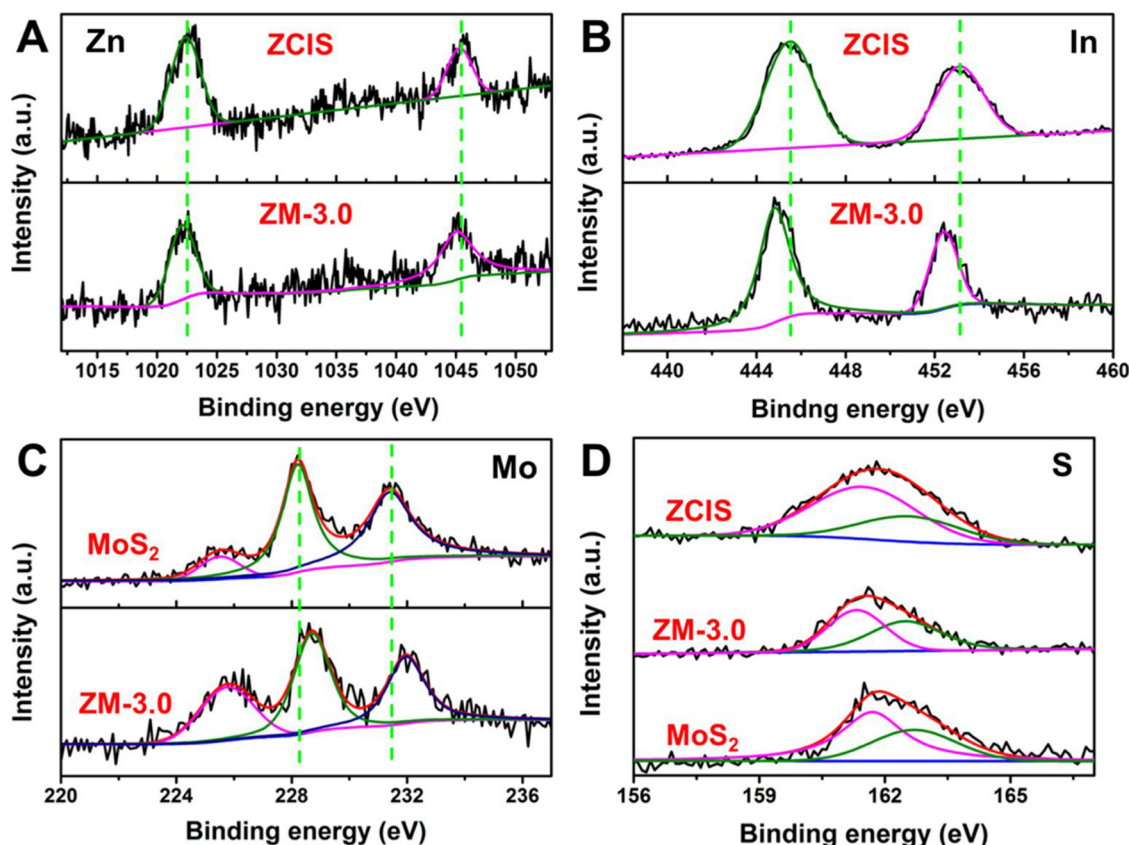
Fig. 3. XPS spectra of Zn 2p (A), In 3d (B), Mo 3d (C), and S 2p (D) in ZCIS, ZM-3.0, and pure MoS_2.

Combination with MoS_2 has a great influence on the optical absorption of samples in longer wavelength region, while affects little on the absorption edge of ZCIS. With increasing the loading amount of MoS_2, light absorption in the range of 600–1100 nm is gradually enhanced, probably due to the increased background absorption because of black colored MoS_2 nanosheets [23,24]. Particularly, all diffuse reflectance spectra show very steep change around 500–600 nm, indicating that the visible-light absorption is attributed to a band transition instead of the transition from impurity levels. The band gap energy of the sample was obtained according to the equation of $\alpha h\nu = A(\alpha h\nu - E_g)^n$, from solid solutions, where h, α, ν, A, and E_g represent Planck's constant, optical absorption coefficient, photon frequency, a constant, and photonic energy band gap, respectively [25]. The band gap of ZCIS is estimated to be 2.28 eV (Fig. S5A). In addition, the band energy position of ZCIS was further determined. As shown in Fig. S5B, the intersection point, corresponding to the flat-band potential E_{fb}, in the Mott-Schottky plots is independent of frequencies, and is calculated to be −1.56 V $vs.$ Ag/AgCl, i.e., −1.36 V $vs.$ normal hydrogen electrode (NHE). The positive slop of Mott-Schottky curve indicates that ZCIS is n-type semiconductors and its E_{fb} is about 0.1 V below the conduction band position (E_{CB}) [26]. Therefore, the E_{CB} position of ZCIS is −1.46 V and its valence band position (E_{VB}) is determined to be 0.82 V.

Photocatalytic H_2 evolution performances of the as-prepared samples were examined under visible light irradiation ($\lambda \geq 420$ nm) with the lactic acid as sacrificial agent. Control experiments suggest that there is no appreciable H_2 generated in the absence of photocatalysts or light irradiation. Fig. 4B shows the average H_2 evolution rate of ZCIS and ZM-X samples. Only a little amount of H_2 is formed from bare ZCIS (0.13 μmol h^{-1}), which is probably due to the fast recombination of photogenerated electron-hole pairs and lack of active sites for photocatalytic reaction. However, a large increase in H_2 evolution rate is observed after combining with MoS_2. The photocatalytic activity of ZM-X is enhanced with the increasing amount of MoS_2 from 0.6 to 3.0 wt%

and the ZM-3.0 sample exhibits the highest H_2 evolution rate (3.5 μmol h^{-1}), which is 27 times higher than that of ZCIS. Further increasing the amount of MoS_2 (ZM-4.2 and ZM-6.0) gives rise to slightly depressed activity but it is still superior to bare ZCIS. The apparent quantum efficiency (AQE) was also estimated to be 0.26% and 8.26% for ZCIS and ZM-3.0, respectively, under the wavelength of 420 ± 5 nm light irradiation. In addition, the H_2 evolution rate of ZM-3.0 after 3 cycles shows negligible decrease (Fig. S6A) and the morphology also has no change (Fig. S6B), indicating a good stability of inherent structure of photocatalyst.

The interfacial charge transfer properties between ZCIS and MoS_2 were first evaluated by a set of photoelectrochemical studies. Electrochemical impedance spectroscopy (EIS) was used to investigate the electrical conductivity of the photocatalysts. In Fig. 4C, ZM-3.0 presents a representative Nyquist plot with a much smaller arc radius than that of other samples, suggesting that the charge transfer resistance is remarkably decreased by introducing a certain amount of MoS_2 [27]. Therefore, the photoinduced electron-hole pairs could separate more efficiently. This conclusion is also supported by transient photocurrent (I-t) curves in Fig. 4D, which shows a much enhanced photocurrent of ZM-3.0 over other samples. It is known that the photocurrent is mainly attributed to the diffusion of photogenerated electrons to the back contact and meanwhile the photogenerated holes are compensated by hole acceptor in the electrolyte [28], the combination of ZCIS and MoS_2 is highly efficient in promoting charge transfer and separation, and thus leads to a better photocatalytic performance as ZM-3.0.

Even though photoelectrochemistry results indicate that the electron transfer resistance is greatly reduced by introduction of MoS_2, it is still necessary to clarify the insight mechanisms and determine the time scale of electron transfer dynamics, rate and efficiency of carrier injection from ZCIS to MoS_2, which are significant and main factors for photocatalytic performance. In this case, time-resolved diffuse
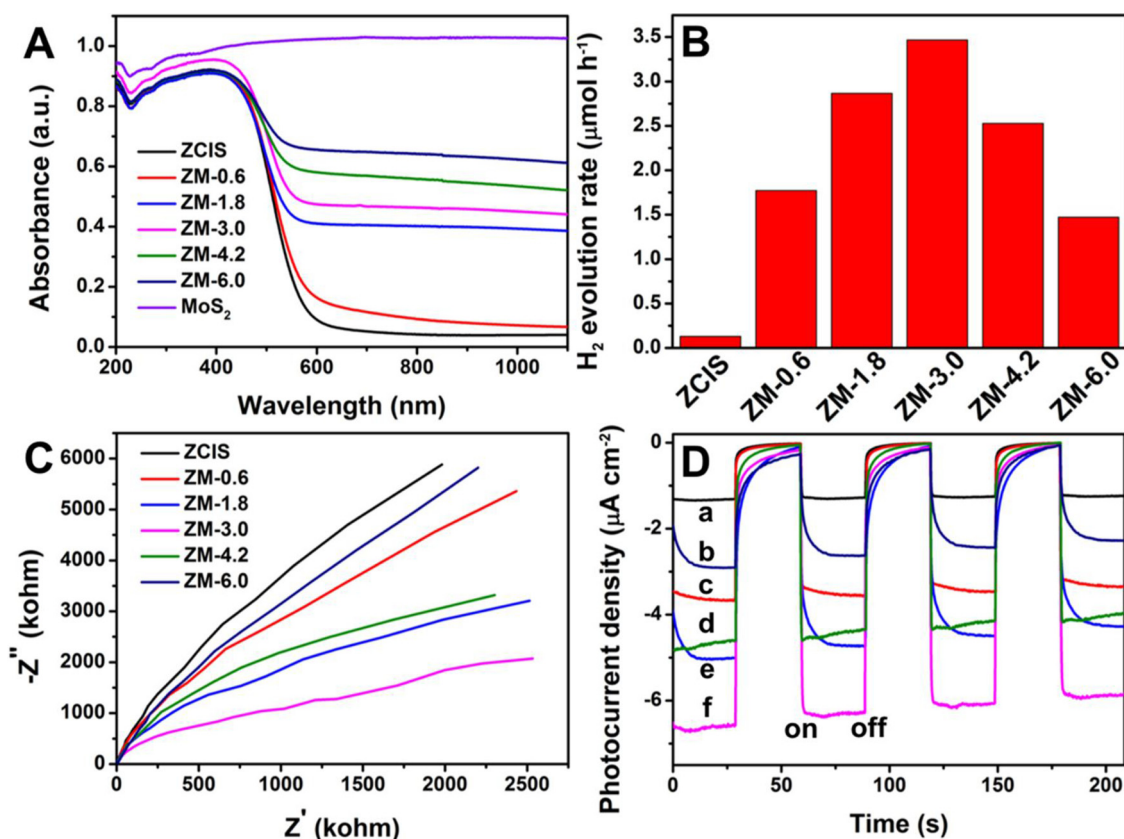
Fig. 4. Diffuse-reflectance spectroscopy of ZCIS, ZM-X, and MoS$_2$ (A). Comparison of photocatalytic H$_2$ evolution activities of ZCIS and ZM-X samples (B). Electrochemical impedance spectroscopy (EIS) Nyquist plots under visible light irradiation (C) and transient photocurrent density curves (D) for ZCIS (a), ZM-6.0 (b), ZM-0.6 (c), ZM-4.2 (d), ZM-1.8 (e), and ZM-3.0 (f) in 0.5 M Na$_2$SO$_4$ solution.
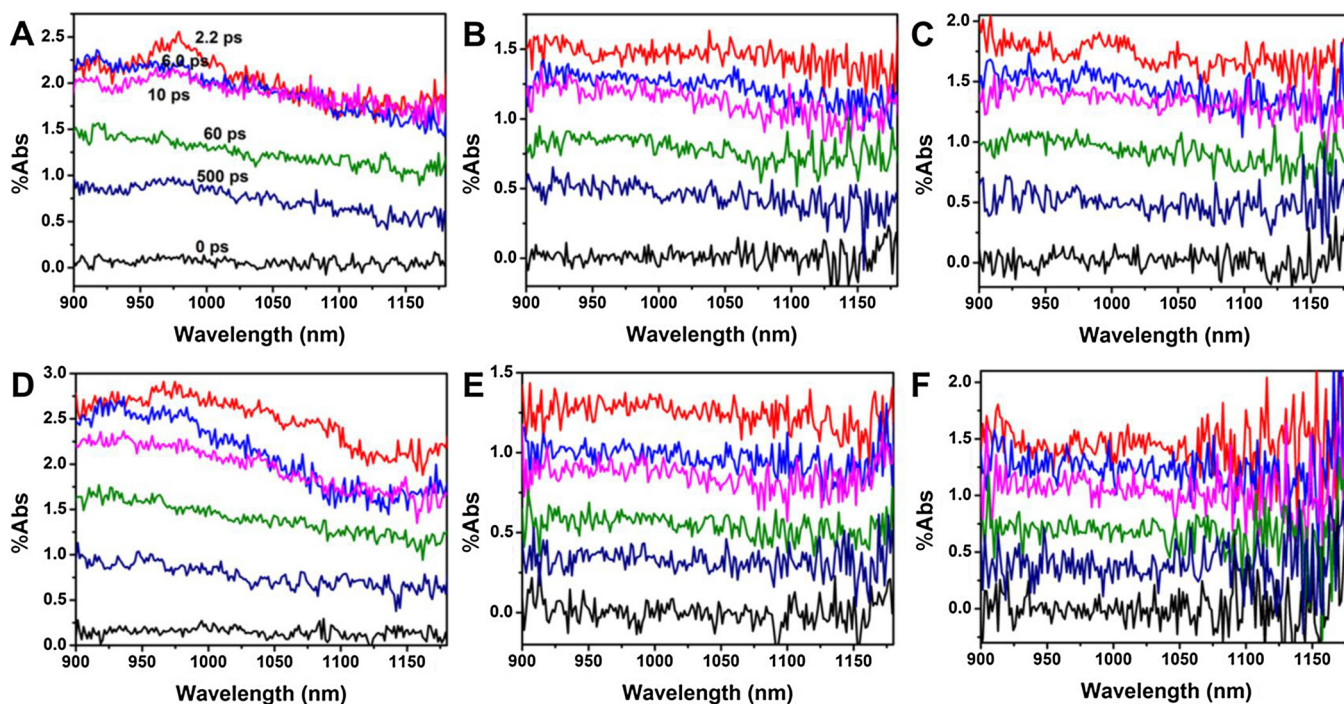

Fig. 5. Time-resolved diffuse reflectance spectra of ZCIS (A), ZM-0.6 (B), ZM-1.8 (C), ZM-3.0 (D), ZM-4.2 (E), and ZM-6.0 (F).

reflectance (TDR) spectroscopy, a powerful analytical tool for investigating ultrafast processes in photocatalysis under various conditions, was employed to directly observe the kinetics of electron

migration after the bandgap excitation. TDR spectra of all photocatalysts were recorded at different time delays after the excitation of samples by 420-nm pulse laser. The spectra reveal a positive absorption
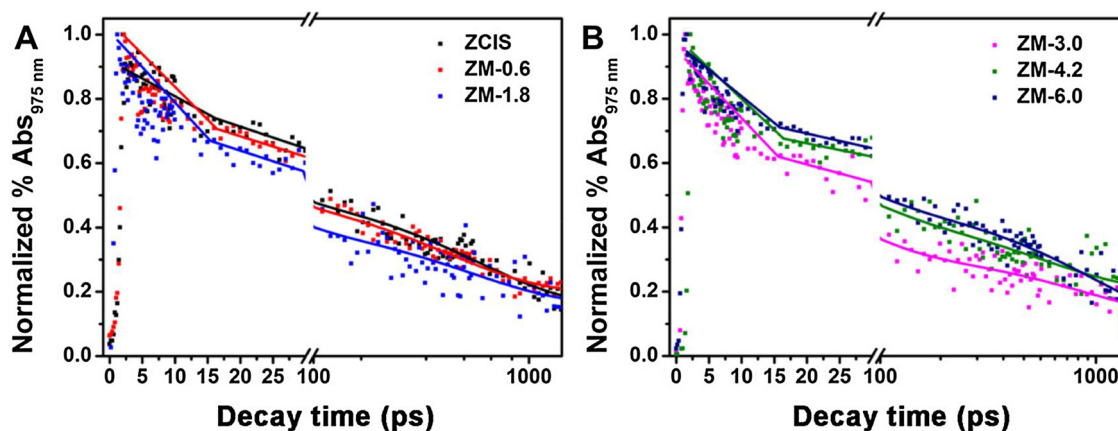
Fig. 6. (A) Time profiles of normalized transient absorption at 975 nm for ZCIS, ZM-0.6, and ZM-1.8 after 420-nm laser irradiation. (B) Time profiles of normalized transient absorption at 975 nm for ZM-3.0, ZM-4.2, and ZM-6.0 after 420-nm laser irradiation.

feature in the wavelength range from 900 to 1180 nm (Fig. 5), which are probably assigned to free and trapped (shallow and deep trapped) photogenerated electrons in ZCIS according to the previous studies [29,30]. Transient absorption intensity of all samples reaches highest immediately after laser flash (< 2 ps) and then gradually decays. Compared with bare ZCIS, the absorption of ZM-X decays more rapidly, and ZM-3.0 exhibits the fastest decay rate. At 10 ps after pulse laser excitation, the absorbance intensities at 975 nm of ZM-X (X = 0.6, 1.8, 3.0, 4.2, and 6.0) show 22.2%, 26.5%, 29.7%, 27.0%, and 22.2% decrease, respectively, which are significantly enhanced compared with bare ZCIS (14.4%). And ZM-3.0 exhibits the fastest decreasing rate. This faster intensity decrease observed with ZM-X indicates the accelerated electron decay kinetics.

Representative decay traces transient absorption at 975 nm are illustrated in Fig. 6 and fitted by a multiexponential function: $\Delta A = \Delta A_0 + \sum_i A_i e^{\left(-\frac{t}{\tau_i}\right)}$, where A and τ refer the amplitudes and lifetimes, respectively [31]. The smallest number of decay lifetimes, τ_i resulted in the minimum χ^2, is used for each fit [32]. Kinetic parameters for these three samples are listed in Table 1. In the case of pure ZCIS, a biexponential decay function is used and the time constants are evaluated to be $\tau_1 = 28.0 \pm 3.4$ ps and $\tau_2 = 580 \pm 139$ ps, which are assigned to electron tapped at defect states and the charge carriers recombination process, respectively [29,33,34]. On the contrary, the decay curves of ZM-X samples are fitted by a triexponential function, demonstrating the existence of an additional deactivation path, i.e., electron transfer process. This extra route is extremely short, less than 5 ps, attributing to the interfacial electron transfer from ZCIS to MoS$_2$ and ZM-3.0 exhibits the fastest electron injection with only 1.12 ps among all ZM-X samples. According to the TEM image, hydrothermal formed MoS$_2$ are mostly deposited on the outside of ZCIS microsphere, therefore, the time constant of several tens picoseconds ($\tau_2 = 26.9 \sim 51.9$ ps) may due to the electrons injection from ZCIS to MoS$_2$ with a long distance or the trapped electrons at defect sites of ZCIS. For the further long-lived component up to several hundred picoseconds, τ_3 is attributed to the slow recombination of photogenerated electron-hole pairs. Based on the fitting data, we calculated the mean

lifetime of the sample according to the equation: $< \tau_{ave} > = \frac{\sum_i A_i \tau_i}{\sum_i A_i}$ [35]. The average lifetime firstly exhibits a sharp decrease from 293 ps (ZCIS) to 87.8 ps (ZM-3.0), and then gradually increase to 178 ps (ZM-6.0). In common, the shorter mean lifetime indicates more rapid the interfacial electron separation. Therefore, this calculated results clearly show that the electrons are injected from ZCIS to MoS$_2$ within a much shorter time scale in ZM-3.0 than other ZM-X samples.

As a more significant parameter for photocatalytic performance, the efficiency of electron injection (η_{inj}) from ZCIS into MoS$_2$ was also acquired as $\eta_{inj} = 1 - \frac{\tau_{ave}(ZM-X)}{\tau_{ave}(ZCIS)}$ [36]. ZM-3.0 also shows the highest injection efficiency (69.9%) than other samples. Considering the different loading amount of MoS$_2$ in ZM-X, this result offers more straightforward and powerful evidence that most efficient transportation of photogenerated electrons between ZCIS and MoS$_2$ happens in ZM-3.0 sample. The electrons injection greatly increases their opportunities to involve into the photocatalysis H$_2$ evolution before the recombination of electron-hole pairs. Therefore, the results of photoelectrochemical and femtosecond time-resolved transient absorption together indicate that the photogenerated electrons could migrate from ZCIS to MoS$_2$, thus to enhance the photocatalytic activity of ZCIS. More importantly, ZM-3.0 shows the fastest electron injection rate and most efficient injection efficiency, which account for its significantly enhanced photocatalytic H$_2$ evolution performance.

Apart from the electrons injection from ZCIS to MoS$_2$ in photocatalysts, the amount of reactive sites in cocatalysts also plays an important role on their photocatalytic H$_2$ evolution activity. According to previous reports, the active sulfur atoms on the exposed edges of MoS$_2$ increase not only its electrocatalytic activity, but also photocatalytic activity [16,37]. These unsaturated active sulfur atoms bind strongly with H$^+$ in solution, which are easily reduced to H$_2$ by electrons. Due to the abundance of H$^+$ ions in lactic acid solution, unsaturated active sulfur atoms on the exposed edges of MoS$_2$ more easily capture H$^+$ ions, thus facilitating H$_2$ generation. Sulfur atoms on the basal plane with three-coordination, however, have no activity [38]. In this case, the enhancing photocatalytic activity from ZM-0.6 to ZM-3.0 is probably

Table 1
Kinetic parameters of transient absorption decays.

| Sample	A_1	A_2	A_3	τ_1 (ps)	τ_2 (ps)	τ_3 (ps)	τ_{ave} (ps)	η_{inj} (%)	χ^2
ZCIS	0.400 (52.0%)	0.369 (48.0%)	–	28.0 ± 3.40	580 ± 139	–	293	–	0.967
ZM-0.6	0.305 (33.4%)	0.388 (42.3%)	0.222 (24.3%)	3.76 ± 0.83	49.3 ± 14.5	555 ± 261	157	46.4	0.970
ZM-1.8	0.706 (53.3%)	0.354 (26.7%)	0.265 (20.0%)	1.25 ± 0.49	33.1 ± 5.50	533 ± 209	116	60.3	0.956
ZM-3.0	1.01 (59.6%)	0.361 (21.3%)	0.324 (19.1%)	1.12 ± 0.35	26.9 ± 3.30	426 ± 66.2	87.8	69.9	0.983
ZM-4.2	0.599 (52.1%)	0.313 (27.2%)	0.238 (20.7%)	2.86 ± 1.00	51.9 ± 9.00	523 ± 186	124	57.7	0.958
ZM-6.0	0.346 (26.0%)	0.573 (43.1%)	0.411 (30.9%)	4.82 ± 1.33	49.6 ± 10.7	503 ± 111	178	39.2	0.980
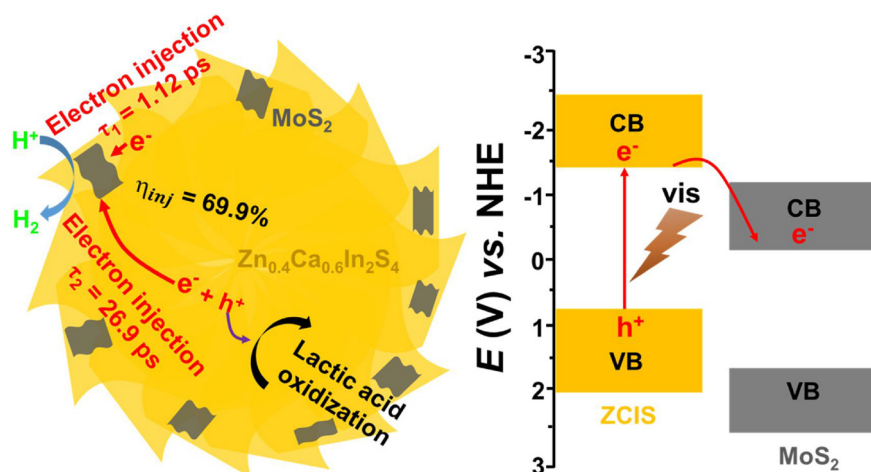
Fig. 7. Schematic illustration of photogenerated charge transfer in ZM-3.0, and the proposed photocatalytic mechanism of H$_2$ evolution.

because of the increasing amount of active sites in MoS$_2$. While with further raising amount of MoS$_2$ to ZM-4.2 and ZM-6.0, aggregated MoS$_2$ nanoflowers start to appear, which greatly decrease the amount of unsaturated sulfur atoms and inhibit the electron mobility [34]. Thereby, ZM-3.0 exhibits the highest activity for photocatalytic H$_2$ generation.

Considering that the CB minimum position of few-layer MoS$_2$ locates at -0.13 V *vs.* NHE together with the above experimental results and analysis, a reasonable charge migration route in ZM-*X* heterostructure and the photocatalytic mechanism for H$_2$ evolution from water is proposed in Fig. 7. Under visible light irradiation, electron-hole pairs are formed and separated in ZCIS microsphere. Some electrons approaching to MoS$_2$ are injected into MoS$_2$ in several picoseconds confirmed by the TDR results. Some other electrons far from MoS$_2$ may transfer to MoS$_2$ within tens picoseconds. These electrons subsequently move to active sites on MoS$_2$ to reduce H$^+$ to H$_2$. At the same time, the photogenerated holes are consumed by hole scavenger. Due to the fast recombination of electron and hole pairs and lack of active sites, however, pure ZCIS possesses a poor H$_2$ evolution activity.

4. Conclusions

In summary, quaternary sulfur semiconductor Zn$_{0.4}$Ca$_{0.6}$In$_2$S$_4$ combined with different amount of layer structured MoS$_2$ are synthesized for visible-light-driven H$_2$ production from water. ZM-3.0 photocatalyst exhibits the maximum H$_2$ evolution rate of 3.5 μmol h^{-1} under visible light irradiation, which is about 27 times higher than that of bare ZCIS. The superior photocatalytic H$_2$ evolution activity of ZM-*X* is ascribed to 2D-2D structure, which greatly increases the contact surface area for charge transfer and supplies more active sites for photocatalytic reaction. The improved charge separation is confirmed by decreasing arc radius of Nyquist plot and significantly enhancement of photocurrent responses. Femtosecond time-resolved diffused reflectance spectroscopy gives a detail information of charge carrier transfer dynamics. It is demonstrated that the electrons could migrate from ZCIS to MoS$_2$ within several picoseconds, causing an efficient charge separation. In addition, the electron injection efficiency in ZM-3.0 is 69.9% and the injection time-scale is the shortest within only 1.12 ps, which are the highest and fastest. Overall, these results suggest that the quaternary sulfur semiconductor can be served as a new kind of photocatalysts for water splitting with the characteristics of visible light responding and environmental friendly.

Conflict of interest

The authors declare no competing financial interest.

Appendix A. Supplementary data

Supplementary material related to this article can be found, in the online version, at doi:https://doi.org/10.1016/j.apcatb.2018.04.054.

References

[1] Y. Hou, B.L. Abrams, P.C. Vesborg, M.E. Björketun, K. Herbst, L. Bech, A.M. Setti, C.D. Damsgaard, T. Pedersen, O. Hansen, Bioinspired molecular co-catalysts bonded to a silicon photocathode for solar hydrogen evolution, Nat. Mater. 10 (2011) 434–438.
[2] H. Tong, S. Ouyang, Y. Bi, N. Umezawa, M. Oshikiri, J. Ye, Nano-photocatalytic materials: possibilities and challenges, Adv. Mater. 24 (2012) 229–251.
[3] J. Zhang, J. Yu, Y. Zhang, Q. Li, J.R. Gong, Visible light photocatalytic H$_2$-production activity of CuS/ZnS porous nanosheets based on photoinduced interfacial charge transfer, Nano Lett. 11 (2011) 4774–4779.
[4] X. Wang, K. Maeda, A. Thomas, K. Takanabe, G. Xin, J.M. Carlsson, K. Domen, M. Antonietti, A metal-free polymeric photocatalyst for hydrogen production from water under visible light, Nat. Mater. 8 (2009) 76–80.
[5] Z. Zhang, J. Huang, J. Fang, M. Zhang, K. Liu, B. Dong, A nonmetal plasmonic Z-scheme photocatalyst with UV-toNIR-driven photocatalytic protons reduction, Adv. Mater. 29 (2017).
[6] R. Asahi, T. Morikawa, H. Irie, T. Ohwaki, Nitrogen-doped titanium dioxide as visible-light-sensitive photocatalyst: designs, developments, and prospects, Chem. Rev. 114 (2014) 9824–9852.
[7] T. Simon, N. Bouchonville, M.J. Berr, A. Vaneski, A. Adrović, D. Volbers, R. Wyrwich, M. Döblinger, A.S. Susha, A.L. Rogach, F. Jäckel, J.K. Stolarczyk, J. Feldmann, Redox shuttle mechanism enhances photocatalytic H$_2$ generation on Ni-decorated CdS nanorods, Nat. Mater. 13 (2014) 1013.
[8] C. Zeng, H. Huang, T. Zhang, F. Dong, Y. Zhang, Y. Hu, Fabrication of heterogeneous-phase solid-solution promoting band structure and charge separation for enhancing photocatalytic CO$_2$ reduction: a case of ZnXCa$_{1-x}$In$_2$S$_4$, ACS Appl. Mater. Interfaces 9 (2017) 27773–27783.
[9] J. Sun, G. Chen, G. Xiong, J. Pei, H. Dong, Hierarchical microarchitectures of AgGa$_{1-x}$In$_x$S$_2$: Long chain alcohol assisted synthesis, band gap tailoring and photocatalytic activities of hydrogen generation, Int. J. Hydrogen Energy 38 (2013) 10731–10738.
[10] S. Ouyang, J. Ye, β-AgAl$_{1-x}$Ga$_x$O$_2$ solid-solution photocatalysts: continuous modulation of electronic structure toward high-performance visible-light photoactivity, J. Am. Chem. Soc. 133 (2011) 7757–7763.
[11] X. Jiao, Z. Chen, X. Li, Y. Sun, S. Gao, W. Yan, C. Wang, Q. Zhang, Y. Lin, Y. Luo, Y. Xie, Defect-mediated electron–hole separation in one-unit-cell ZnIn$_2$S$_4$ layers for boosted solar-driven CO$_2$ reduction, J. Am. Chem. Soc. 139 (2017) 7586–7594.
[12] Y.-J. Yuan, D. Chen, J. Zhong, L.-X. Yang, J. Wang, M.-J. Liu, W.-G. Tu, Z.-T. Yu, Z.-G. Zou, Interface engineering of a noble-metal-free 2D-2D MoS$_2$/Cu-ZnIn$_2$S$_4$ photocatalyst for enhanced photocatalytic H$_2$ production, J. Mater. Chem. A 5 (2017)

15771–15779.

[13] K. Chang, Z. Mei, T. Wang, Q. Kang, S. Ouyang, J. Ye, MoS_2/Graphene cocatalyst for efficient photocatalytic H_2 evolution under visible light irradiation, ACS Nano 8 (2014) 7078–7087.

[14] Y. Li, H. Wang, L. Xie, Y. Liang, G. Hong, H. Dai, MoS_2 nanoparticles grown on graphene: an advanced catalyst for the hydrogen evolution reaction, J. Am. Chem. Soc. 133 (2011) 7296–7299.

[15] H.I. Karunadasa, E. Montalvo, Y. Sun, M. Majda, J.R. Long, C.J. Chang, A molecular MoS_2 edge site mimic for catalytic hydrogen generation, Science 335 (2012) 698–702.

[16] K. Chang, M. Li, T. Wang, S. Ouyang, P. Li, L. Liu, J. Ye, Drastic layer-number-dependent activity enhancement in photocatalytic H_2 evolution over $nMoS_2$/CdS ($n \geq 1$) under visible light, Adv. Energy Mater. 5 (2015) 1402279.

[17] B. Hinnemann, P.G. Moses, J. Bonde, K.P. Jørgensen, J.H. Nielsen, S. Horch, I. Chorkendorff, J.K. Nørskov, Biomimetic hydrogen evolution: MoS_2 nanoparticles as catalyst for hydrogen evolution, J. Am. Chem. Soc. 127 (2005) 5308–5309.

[18] W. Zhou, Z. Yin, Y. Du, X. Huang, Z. Zeng, Z. Fan, H. Liu, J. Wang, H. Zhang, Synthesis of few-layer MoS_2 nanosheet-coated TiO_2 nanobelt heterostructures for enhanced photocatalytic activities, Small 9 (2013) 140–147.

[19] R. Godin, Y. Wang, M.A. Zwijnenburg, J. Tang, J.R. Durrant, Time-resolved spectroscopic investigation of charge trapping in carbon nitrides photocatalysts for hydrogen generation, J. Am. Chem. Soc. 139 (2017) 5216–5224.

[20] S.R. Pendlebury, X. Wang, F. Le Formal, M. Cornuz, A. Kafizas, S.D. Tilley, M. Gratzel, J.R. Durrant, Ultrafast charge carrier recombination and trapping in hematite photoanodes under applied bias, J. Am. Chem. Soc. 136 (2014) 9854–9857.

[21] X.B. Li, Y.J. Gao, Y. Wang, F. Zhan, X.Y. Zhang, Q.Y. Kong, N.J. Zhao, Q. Guo, H.L. Wu, Z.J. Li, Y. Tao, J.P. Zhang, B. Chen, C.H. Tung, L.Z. Wu, Self-assembled framework enhances electronic communication of ultrasmall-sized nanoparticles for exceptional solar hydrogen evolution, J. Am. Chem. Soc. 139 (2017) 4789–4796.

[22] W. Yin, L. Bai, Y. Zhu, S. Zhong, L. Zhao, Z. Li, S. Bai, Embedding metal in the interface of a p-n heterojunction with a stack design for superior Z-Scheme photocatalytic hydrogen evolution, ACS Appl. Mater. Interfaces 8 (2016) 23133–23142.

[23] X. Shi, M. Fujitsuka, S. Kim, T. Majima, Faster electron injection and more active sites for efficient photocatalytic H_2 evolution in g-C_3N_4/MoS_2 hybrid, Small 14 (2018) 1703277.

[24] M.-Q. Yang, C. Han, Y.-J. Xu, Insight into the effect of highly dispersed MoS_2 versus layer-structured MoS_2 on the photocorrosion and photoactivity of CdS in Graphene–CdS–MoS_2 composites, J. Phys. Chem. C 119 (2015) 27234–27246.

[25] Y. Li, R. Jin, Y. Xing, J. Li, S. Song, X. Liu, M. Li, R. Jin, Macroscopic foam-like holey ultrathin g-C_3N_4 nanosheets for drastic improvement of visible-light photocatalytic activity, Adv. Energy Mater. 6 (2016) 1601273.

[26] C. Zeng, Y. Hu, H. Huang, $BiOBr_{0.75}I_{0.25}$/$BiOIO_3$ as a novel heterojunctional photocatalyst with superior visible-light-driven photocatalytic activity in removing diverse industrial pollutants, ACS Sustainable Chem. Eng. 5 (2017) 3897–3905.

[27] X. Zhu, P. Wang, Q. Zhang, Z. Wang, Y. Liu, X. Qin, X. Zhang, Y. Dai, B. Huang, CdS-MoS_2 heterostructures on Mo substrates via in situ sulfurization for efficient photoelectrochemical hydrogen generation, RSC Adv. 7 (2017) 44626–44631.

[28] L. Yuan, M.-Q. Yang, Y.-J. Xu, A low-temperature and one-step method for fabricating $ZnIn2S_4$-GR nanocomposites with enhanced visible light photoactivity, J. Mater.Chem. A 2 (2014) 14401–14412.

[29] J. Ravensbergen, F.F. Abdi, J.H. van Santen, R.N. Frese, B. Dam, R. van de Krol, J.T.M. Kennis, Unraveling the carrier dynamics of $BiVO_4$: a femtosecond to microsecond transient absorption study, J. Phys. Chem. C 118 (2014) 27793–27800.

[30] Z. Bian, T. Tachikawa, P. Zhang, M. Fujitsuka, T. Majima, Au/TiO_2 superstructure-based plasmonic photocatalysts exhibiting efficient charge separation and unprecedented activity, J. Am. Chem. Soc. 136 (2014) 458–465.

[31] I. Grigioni, K.G. Stamplecoskie, E. Selli, P.V. Kamat, Dynamics of photogenerated charge carriers in WO_3/$BiVO_4$ heterojunction photoanodes, J. Phys. Chem. C 119 (2015) 20792–20800.

[32] C.C. Milleville, K.E. Pelcher, M.Y. Sfeir, S. Banerjee, D.F. Watson, Directional charge transfer mediated by mid-gap States: a transient absorption spectroscopy study of CdSe quantum Dot/β-$Pb_{0.33}V_2O_5$heterostructures, J. Phys. Chem. C 120 (2016) 5221–5232.

[33] X.-L. Yin, G.-Y. He, B. Sun, W.-J. Jiang, D.-J. Xue, A.-D. Xia, L.-J. Wan, J.-S. Hu, Rational design and electron transfer kinetics of MoS_2/CdS nanodots-on-nanorods for efficient visible-light-driven hydrogen generation, Nano Energy 28 (2016) 319–329.

[34] X. Shi, M. Fujitsuka, Z. Lou, P. Zhang, T. Majima, In situ nitrogen-doped Hollow-TiO_2/g-C_3N_4 Composite photocatalysts with efficient charge separation boosting water reduction under visible light, J. Mater. Chem. A 5 (2017) 9671–9681.

[35] W.-J. Ong, L.K. Putri, Y.-C. Tan, L.-L. Tan, N. Li, Y.H. Ng, X. Wen, S.-P. Chai, Unravelling charge carrier dynamics in protonated g-C_3N_4 interfaced with carbon nanodots as co-catalysts toward enhanced photocatalytic CO_2 reduction: a combined experimental and first-principles DFT study, Nano Res. 10 (2017) 1673–1696.

[36] M. Abdellah, K. Žídek, K. Zheng, P. Chábera, M.E. Messing, T. Pullerits, Balancing electron transfer and surface passivation in gradient CdSe/ZnS core–shell quantum dots attached to ZnO, J. Phys. Chem. Lett. 4 (2013) 1760–1765.

[37] X.-Y. Yu, H. Hu, Y. Wang, H. Chen, X.W. Lou, Ultrathin MoS_2 nanosheets supported on n-doped carbon nanoboxes with enhanced lithium storage and electrocatalytic properties, Angew. Chem. Int. Ed. 54 (2015) 7395–7398.

[38] M.A. Lukowski, A.S. Daniel, F. Meng, A. Forticaux, L. Li, S. Jin, Enhanced hydrogen evolution catalysis from chemically exfoliated metallic MoS_2 nanosheets, J. Am. Chem. Soc. 135 (2013) 10274–10277.